Flow (2025), **5** E21
doi:10.1017/flo.2025.16

FLOW CAMBRIDGE UNIVERSITY PRESS

RESEARCH ARTICLE

Assessment of mixing efficiency of thermally driven microfluidic swirlers

Filippo Azzini[1], Amira M'hadbi[2], Mohammed El Ganaoui[2], Beatrice Pulvirenti[1], Gian Luca Morini[1], Marcos Rojas-Cárdenas[3] and Massimiliano Rossi[1]

[1]Department of Industrial Engineering, Alma Mater Studiorum Università di Bologna, Bologna, Italy
[2]LERMAB, Department of Transition and Energy Efficiency Professions, IUT de Longwy, University of Lorraine, Longwy, France
[3]Institut Clément Ader (ICA), CNRS, INSA, ISAE-SUPAERO, Mines-Albi, UPS, Université de Toulouse, Toulouse, France
Corresponding author: Massimiliano Rossi; Email: massimiliano.rossi13@unibo.it

Received: 11 December 2024; **Revised:** 26 March 2025; **Accepted:** 16 April 2025

Keywords: defocus particle tracking; microfluidics; micromixers; mixed convection; thermally-driven microfluidic swirler

Abstract

In this study, we examine the mixing performance of thermally induced microfluidic swirlers, which are recently developed micromixers based on mixed thermal convection. In this configuration, a swirling flow motion is induced by the combination of natural convection and a pressure-driven Poiseuille flow. An experimental investigation was carried out on a microfluidic swirler composed of a glass capillary with a square cross-section of 800×800 μm^2, measuring the three-dimensional flow fields in different operating conditions using the general defocusing particle tracking technique. Furthermore, a thorough numerical analysis was performed to characterise the mixing performance for different Reynolds numbers and microchannel dimensions. Our results show that thermally induced microfluidic swirlers have an optimal range of operation for microchannel with hydraulic diameters between 400 and 1600 μm and Reynolds numbers around 1, where they show an increase of mixing efficiency up to 60 % with respect to the case of pure diffusion. The swirl is activated already at moderate temperature differences of 20–30 K, making this approach compatible with most chemical and biomedical applications.

Impact Statement

Thermally induced microfluidic swirlers are recent microdevices that use mixed convection as a mechanism for the enhancement of heat and mass transfer. Despite its simplicity and robustness, this concept of micromixing is still largely unexplored. This could be due to the common assumption that buoyancy forces are negligible in microfluidics, or that temperature gradients could be harmful, for instance, in biomedical applications. In this work, we show both experimentally and numerically, that mixed convection has an optimal range of operation with respect to mixing in a microchannel with dimensions between 400 and 1600 μm working at Reynolds number around 1. In these conditions, small temperature differences between 20 and 30 K are sufficient to establish a consistent swirling motion that enhances mixing. These findings can have a significant scientific impact by providing quantitative data on the mixing efficiency of mixed convection in microfluidics. From a technological point of view, our results demonstrate that thermally induced microfluidic swirlers are a viable solution to achieve low-cost, effective, active micromixers.

1. Introduction

Mixing has been identified as one of the major challenges in microfluidic devices since the emergence of this research field more than two decades ago (Whitesides 2006). The reason is that the absence of

turbulent mixing at the small scales makes the mixing of different fluids, chemicals or molecules in microfluidic channels very slow since it must rely only on diffusion. One of the first strategies proposed to enhance mixing in microchannels was the use of geometrical modifications or obstacles to disrupt fluid motion, creating a transverse flow field that stretches and extends the interface between the mixing fluids, thus increasing the contact area where diffusion acts. Some notable examples are the seminal work of Stroock *et al*. (2002) on chaotic mixers based on bas-relief structures or ridges on the channel floor or the use of secondary flow occurring in curvilinear channels (Jiang *et al*. 2004; Schönfeld & Hardt 2004). These studies showed important results for a wide range of Reynolds numbers and inspired follow-up works with different concepts like the split-and-recombine technique (Hardt *et al*. 2006), where the contact surface is exponentially increased and the length path is decreased to reduce the mixing time (Capretto *et al*. 2011). Other designs of a micromixer include specially designed structures such as curved microchannels (Picardo & Pushpavanam 2015), gear-shaped microchannels (Hong *et al*. 2021), serpentine microchannels (Zhang *et al*. 2019), the T-junction and Y-junction (Hsieh *et al*. 2013; Wang *et al*. 2012) and obstacle-based design (Amar *et al*. 2020; Ansari *et al*. 2018; Milotin & Lelea 2016). All of these designs fall into the category of passive micromixers, which operate without any external energy input and rely solely on the pressure difference that drives fluid flow at a constant rate. In contrast to passive mixers, active micromixers employ various external energy sources to enhance and control mixing within microchannels. In this case, for expanding the contact area between fluids, disrupting fluid flows or initiating chaotic advection, different types of energy sources can be used including pressure fields (Li & Kim 2017), electric fields (Ebrahimi *et al*. 2014), magnetic fields (Bayareh *et al*. 2019), thermal fields (Tan 2019), acoustic fields (Lim *et al*. 2019) and oscillating bubbles (Rallabandi *et al*. 2017), among others. For a more comprehensive list of passive and active micromixer designs and approaches, we refer the reader to recent review papers (Cai *et al*. 2017; Li *et al*. 2022).

While many of these approaches have been studied extensively in the past years, micromixers based on mixed thermal convection, which occurs when both mechanisms of natural and forced convection act on a fluid, are largely unexplored at the microfluidic scale (Ward & Fan 2015). This might be due to the fact that temperature-driven buoyancy forces are commonly considered negligible in microfluidics, leading to the overlook of this approach. Kim *et al*. (2009) proposed a simple-to-implement device for both mixing and polymerase chain reaction based on natural convection occurring in a closed cavity. More recently, Ishii *et al*. (2018) investigated, through both experimental and numerical (Ishii *et al*. 2020) methods, the fluid flows in a T-shaped microchannel where two fluids are mixed when a temperature gradient is applied. The temperature effect generates a strong spiral flow in the channel. The numerical study clarified that this mechanism was driven by natural convection due to temperature differences rather than inlet velocities. Zhang *et al*. (2020) analysed the performance of a micromixer that used a microheater made of indium tin oxide to generate buoyancy effects within the fluid.

In general, it has been shown that moderate temperature gradients can be used to establish swirling flows in microfluidic devices. Furthermore, from a fabrication point of view, this class of active mixers is particularly interesting since it does not require movable parts and can easily be implemented in several microfluidic device architectures. However, the studies currently available in the literature cover relatively small operational ranges, and a systematic analysis that can assess the effective mixing efficiency of mixed convection at the microfluidic scale is still missing. This information is critical to identify the useful range of operation of these devices and to compare the performance with different mixing strategies.

In this work, we intend to fill this gap by systematically investigating, experimentally and numerically, the performance of a thermally induced microfluidic swirler. In comparison with existing studies, we significantly extend the parameter space, covering hydraulic diameters from 0.1 to 2 mm and Reynolds numbers from 0.1 to 10.0. The analysis is performed on straight microchannels with squared cross-sections to solely characterise the effect of mixed convection without additional contributions that could arise from T-shaped inlets or more complex geometries. Furthermore, the experimental flow measurements are performed with a three-dimensional (3-D) particle tracking technique for microfluidics, which is able to directly capture the 3-D nature of the swirling flow.

https://doi.org/10.1017/flo.2025.16 Published online by Cambridge University Press

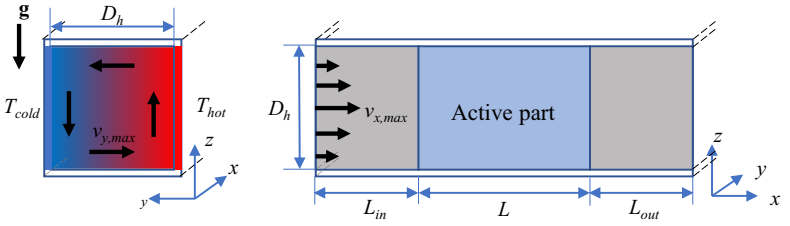

Figure 1. *Principle of microfluidic mixers based on mixed thermal convention. A natural thermal convection flow is established in the transverse direction, driven by a horizontal temperature gradient and buoyancy forces. Forced convection is established in the streamwise direction by imposing a pressure–driven flow. The magnitude of the transverse (natural convection) and streamwise (forced) flow are characterised in terms of the maximum velocity components* $|v_y|_{\max}$ *and* $|v_x|_{\max}$*, respectively.*

The paper is organised as follows. In Section 2 the general description of the geometrical domain and the working principle are summarised. Section 3 focuses on the experimental assessment, comparing the flow field obtained using general defocus particle tracking (GDPT) Barnkob *et al*. (2015), a 3-D particle tracking technique for microfluidics. In Section 4, the numerical assessment is presented, based on systematic numerical simulations for different Reynolds numbers and microchannel dimensions. Conclusions and future recommendations are presented in Section 5.

2. Fundamentals of thermally driven microfluidic swirlers

The working principle of a thermally driven microfluidic swirler with the specific geometrical conventions used in this study is presented in figure 1. The coordinate system is arranged with the x, y and z axes aligned with respect to the microchannel's length (streamwise direction), width and height, respectively. We consider microchannels with a square cross-section, thus with a hydraulic diameter, D_h, corresponding to the side length. Two different temperatures, namely T_{hot} and T_{cold} (with $T_{hot} > T_{cold}$), are imposed on the sidewalls at $y = -D_h/2$ and $y = +D_h/2$, respectively. This configuration creates a temperature gradient within the fluid perpendicular to the gravity vector $\mathbf{g}$ (here directed along the z direction). Consequently, the buoyancy forces generated within the fluid establish a natural convection flow that, in the present configuration, takes the form of a transverse vortex, with the fluid moving upward at the hot side and downward at the cold side. Forced convection in the perpendicular, streamwise direction is established by imposing a pressure-driven Poiseuille flow.

A technologically important aspect of this approach is that it works particularly well on the microfluidic scale on devices working at low flow rates. In typical microfluidic geometries, with microchannel diameters of the order of hundreds of micrometres, the magnitude of the natural convection flow established with temperature differences around 10–50 K is of the same order of magnitude as the typical velocities of pressure-driven flow (10–100 μm/s). For smaller dimensions, the convective flow becomes negligible, and this approach cannot be used. For larger geometries and flow velocities, it is easier to promote the mixing with different strategies such as flow instabilities and chaotic advection. The temperature gradient can easily be established with Peltier modules embedded in the microfluidic device, and the required small temperature gradients are compatible with most biological applications. This makes this approach particularly suitable for a wide range of microfluidic and lab-on-a-chip applications.

In the following experimental and numerical analysis, the magnitude of the transverse natural convection flow and of the streamwise pressure-driven flow is evaluated quantitatively in terms of the maximum velocity components $|v_y|_{\max}$ and $|v_x|_{\max}$, respectively.

3. Experimental analysis

In this section, we present the experimental assessment of the mixing performance of a microfluidic active mixer based on the mixed thermal convection principle. The analysis is performed on a single geometric configuration and for different Reynolds numbers and temperature differences. The results are used as a validation for the follow-up numerical analysis on a more extended parameter space.

https://doi.org/10.1017/flo.2025.16 Published online by Cambridge University Press

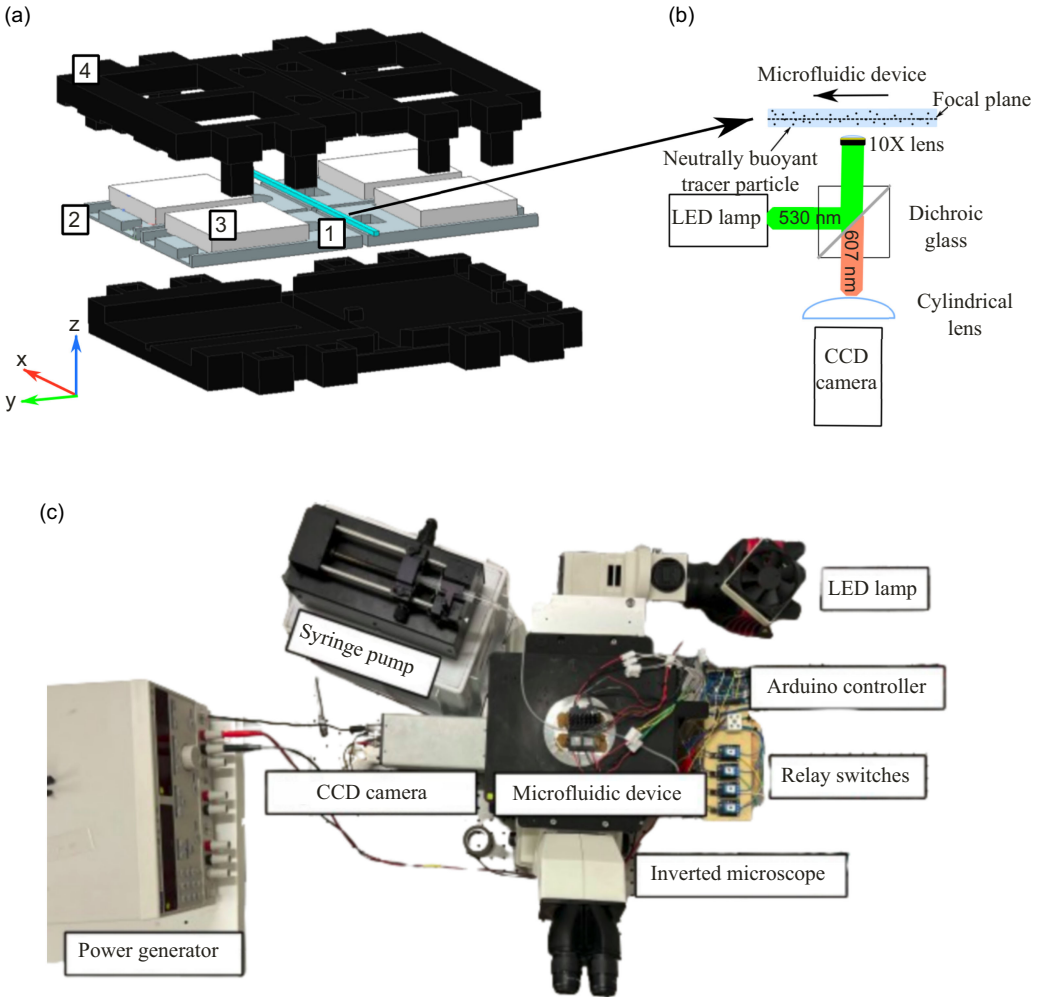

Figure 2. *(a) Exploded view of the microfluidic device used in the experimental campaign; (b) schematic representation of the optical systems used; (c) experimental apparatus used in this work.*

3.1. Microfluidic chip

The microfluidic chip, schematically depicted in figure 2a is designed to investigate the effect of different temperature gradients on fluid motion. Four Peltier modules are employed to establish the temperature gradient. Each module is connected to a power generation unit and regulated via an Arduino-UNO microcontroller. The microcontroller is interfaced with five negative-temperature-coefficient (NTC) thermistors, four of which are put in contact with each Peltier module to measure their individual temperatures, the fifth being deployed to monitor the ambient temperature. The microcontroller acts on four relay switches that control the Peltier modules by a sequence of ON/OFF cycles to maintain the desired set-point temperatures (T_{hot} and T_{cold}), with this approach, the temperature is maintained around the set-point values with a deviation of ± 0.5 K.

The microfluidic chip is composed of a capillary glass tube (VitroTubes, VitroCOM) with a square cross-section of 800×800 μm^2 and a length of 50 mm (1). The external sidewalls of the capillary are put in contact with four *ad hoc* 3D-printed aluminium cases (2) used to facilitate the heat transfer between the Peltier modules (3) and the capillary walls. All the components were assembled together in a 3D-printed polylactic acid case (4). A syringe pump (Harvard PHD 4400) was used to impose the streamwise, pressure-driven Poiseuille flow in the microchannel. The string pump is driven by a

https://doi.org/10.1017/flo.2025.16 Published online by Cambridge University Press

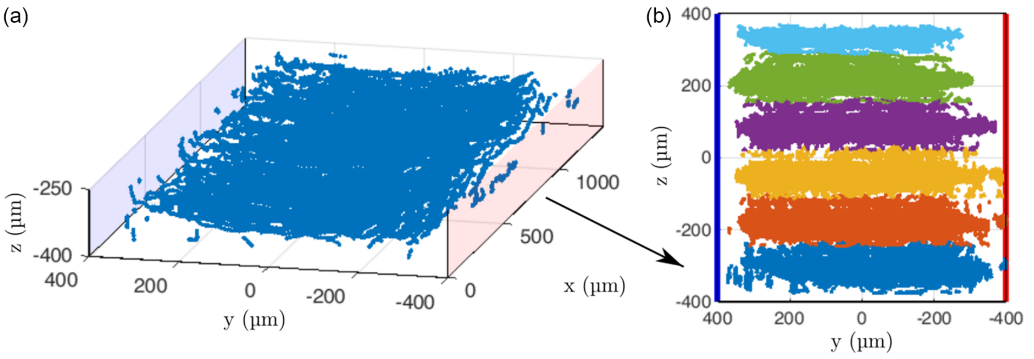

Figure 3. *(a) Single measurement obtained with GDPT corresponding to a* $1400 \times 800 \times 100 \mu m^3$ *measurement volume. Tracer particle trajectories were collected through 200 image recordings taken at 8.16 Hz. (b) Six measurement volumes were considered across the microchannel height with a spacing of 100 μm. The y-axis is plotted with direction from right to left for consistency with the 3-D plots.*

stepper motor that can generate small periodic fluctuations in the streamwise flow velocity at low flow rates. The impact of these fluctuations in our analysis will be discussed in detail in the results section. The whole experimental apparatus was mounted on an inverted microscope (Nikon Eclipse TE2000-U) during operation to allow the flow velocity measurements and it is shown in figure 2c.

3.2. General defocus particle tracking

The 3-D flow field in the microchannel was measured using GDPT (Barnkob *et al*. 2015; Barnkob & Rossi 2020), a well-established single-camera method in which the depth position of the particles (i.e. parallel to the optical axis of the microscope objective) is determined by the defocusing pattern of the corresponding particle images.

The optical and image acquisition system is composed of the epi-fluorescent inverted microscope coupled to a high-sensitivity CCD camera (PCO SensiCam). A sketch of the optical system is presented in figure 2b. A high-power LED (Solis 525C, Thorlabs) emits green light with a wavelength of 525 nm. Thanks to a dichroic mirror, the light is directed to the microfluidic device through a 10× objective lens with a numerical aperture NA = 0.25. Here, the fluorescent tracer microparticles absorb the green light and re-emit it at 607 nm. This emitted light passes through the dichroic mirror and reaches the CCD sensor of the camera. An additional cylindrical lens placed in front of the sensor induces astigmatic aberration in the defocused particle images, providing more efficient and unambiguous encoding of defocusing information for depth position determination (Barnkob *et al*. 2021). Polystyrene microparticles with a diameter of 5.0 μm and density of 1050 kg/m^3 (Microparticles GmbH) were used as tracer particles in the flow at low concentration. The images were processed using the open-source software *DefocusTracker* (Barnkob & Rossi 2021).

With this configuration, we achieved a measurement volume of approximately $1400 \times 800 \times 100$ μm^3 (length × width × height). To cover the entire volume of the channel, six measurement volumes across the microchannel channel height, spaced with a distance of 100 μm, were measured for each experimental case, as reported in figure 3. For each case, 200 images were recorded at a frame rate of 8.16 Hz. The estimated uncertainty in the determination of the position of individual particles was approximately 0.2 μm in the in-plane direction and 3 μm in the out-of-plane direction (Barnkob & Rossi 2020). The particle trajectories were calculated using a nearest-neighbour scheme, and a smoothing step based on the locally weighted scatter plot smooth (loess) method across 5 consecutive data points was applied to reduce the random velocity errors. A further correction procedure based on a reference measurement of a Poiseuille flow was applied to reduce the bias error resulting from the field curvature aberration and refractive index mismatch (Coutinho *et al*. 2023). The final uncertainty in the velocity measurement

https://doi.org/10.1017/flo.2025.16 Published online by Cambridge University Press

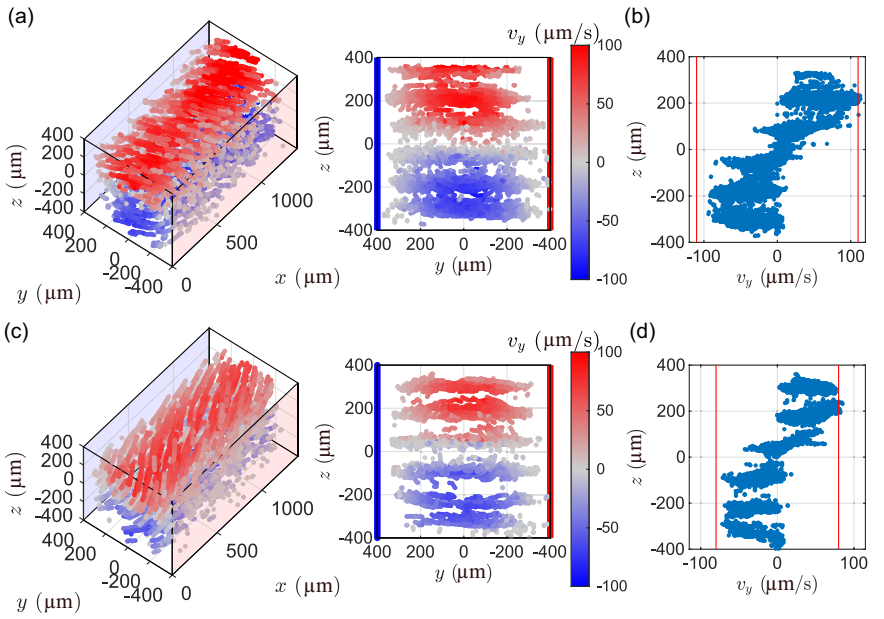

Figure 4. *(a) Tracer particle trajectories measured in a swirling flow without the pressure-driven flow (Q = 0 ml/h) and a temperature difference ΔT = 30 K. (b) Corresponding velocity profile across the depth direction of the horizontal velocity component, v_y. (c) Tracer particle trajectories measured in a swirling flow with the pressure-driven flow (Q = 0.2 ml/h) and a temperature difference ΔT = 30 K. (d) Corresponding velocity profile across the depth direction of the horizontal velocity component, v_y. The missing data correspond to regions outside the measurement volumes.*

estimated on straight trajectories was approximately 2 and 8 μm/s for the in-plane and out-of-plane directions, respectively.

3.3. Experimental results

The experimental analysis focuses on the fluid flow motion under different temperature gradients and on the case of pure natural convection (without pressure-driven flow) and mixed convection (pressure-driven flow with a constant flow rate of Q = 0.2 ml/h). We perform in total 12 different experiments, considering 6 temperature differences between the two walls of the microchannel, corresponding to ΔT = 5, 10, 15, 20, 25, 30 K. A representative result of the GDPT measurement for ΔT = 30 K between the sidewalls is presented in figure 4, with and without the super-imposed pressure-driven flow.

The cold and hot walls are drawn in blue and red, respectively. The colour coding of the trajectories represents the value of the transverse velocity v_y. In the case of natural convection (Figure 4a), the trajectories are confined in a plane approximately perpendicular to the channel axis. The projection of the trajectories in the yz-plane shows clearly the convection vortex, with a magnitude of approximately $|v_y|_{max} \simeq 90$ μm/s. In the case with mixed convection (Figure 4b), the flow in the streamwise direction corresponds to a parabolic Poiseuille flow, with a maximum streamwise velocity of $|v_x|_{max} \simeq 180$ μm/s, and a buoyancy-driven vortex in the transverse direction, with a maximum magnitude of $|v_y|_{max} \simeq 65$ μm/s. The corresponding trajectories are, therefore, arranged in a helical motion. A point to consider is that the estimated sedimentation velocity of the 5-μm-diameter polystyrene tracer particles in water, across the temperature ranges observed in the experiments, varies from 0.52 to 1.37 μm/s. These values are small compared with the transverse velocities, but not negligible, especially for the cases with ΔT = 5 K. To avoid possible bias errors in the evaluation of the magnitude of the transverse velocity, we chose to estimate it in terms of the y-component, $|v_y|_{max}$, which is perpendicular to the gravitational acceleration and not directly affected by sedimentation.

https://doi.org/10.1017/flo.2025.16 Published online by Cambridge University Press

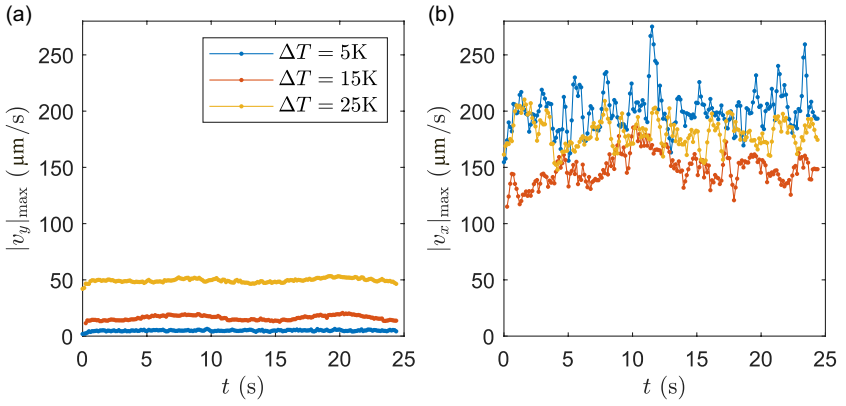

Figure 5. *Maximum value of the y and x components of velocity obtained for three different temperature differences (ΔT = 5, 15 and 25 K), plotted as a function of time.*

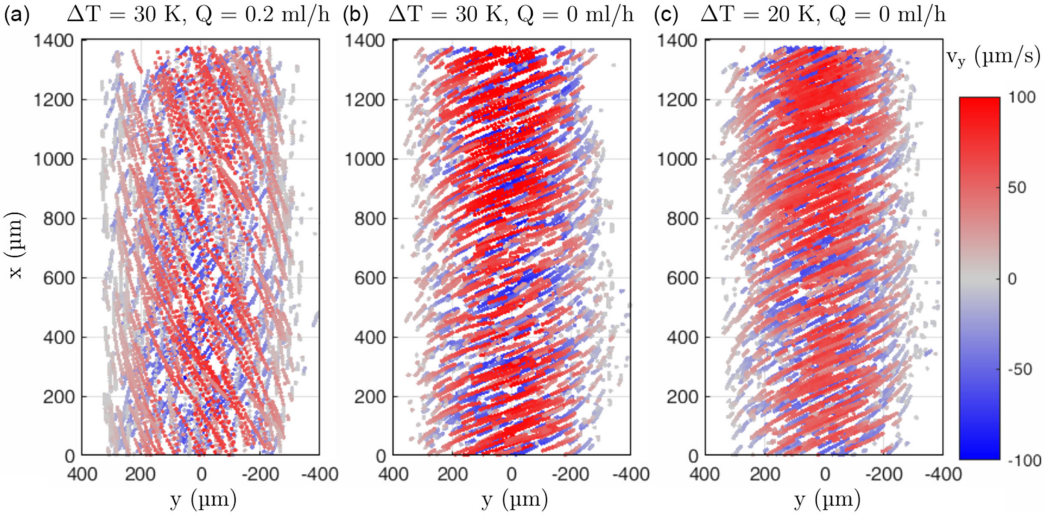

Figure 6. *Top view of the particles trajectories in different cases: (a) ΔT = 30 K and Q = 0.2 ml/h; (b) ΔT = 30 K and Q = 0.0 ml/h; (c) ΔT = 20 K and Q = 0.0 ml/h.*

Several interesting phenomena emerge from the experimental analysis. First, as shown in figure 5, the actual streamwise velocity imposed by the syringe pump oscillates significantly around its nominal value (corresponding to Q = 0.2 ml/h) due to the working principle and limitation of the syringe pump used. These oscillations can reach up to 50 µm/s above the mean value. On the other hand, the transverse velocity, driven by the buoyancy forces and by the thermal gradient steadily controlled by the Peltier elements, remains stable with no appreciable fluctuations, independently of the applied.

A second observation is that the plane of the buoyancy-driven transverse vortex in the natural convection case is not perfectly perpendicular to the channel streamwise axis, as could be expected from symmetry reasons. This could be explained by a slight tilt of the channel axis with respect to the gravity vector, i.e. the microfluidic device or the microscope stage was not perfectly horizontal. This explanation is supported by the fact that the tilting angle stays approximately constant also for different temperature differences and vortex magnitude, as shown in figure 6b–c from the top view of the trajectories presented for ΔT = 30 K and ΔT = 20 K.

Another aspect to consider concerns the magnitude of the transverse vortices which is, as expected, proportional to the imposed ΔT. However, for the cases without the pressure-driven flow, given the same magnitude of the temperature gradient, the magnitude of the transverse flow is larger with respect

https://doi.org/10.1017/flo.2025.16 Published online by Cambridge University Press

Table 1. *Values of Re, Gr, Ri and velocity ratio v^* for the investigated experimental condition. The flow rate is constant for all cases at Q = 0.2 ml/h*

ΔT	Re	Gr	Ri	v^*
5 K	0.079	2.5	1250	0.026
10 K	0.084	22	3118	0.048
15 K	0.089	41.5	5239	0.089
20 K	0.094	61	6904	0.168
25 K	0.099	94.5	9642	0.26
30 K	0.104	128	11834	0.358

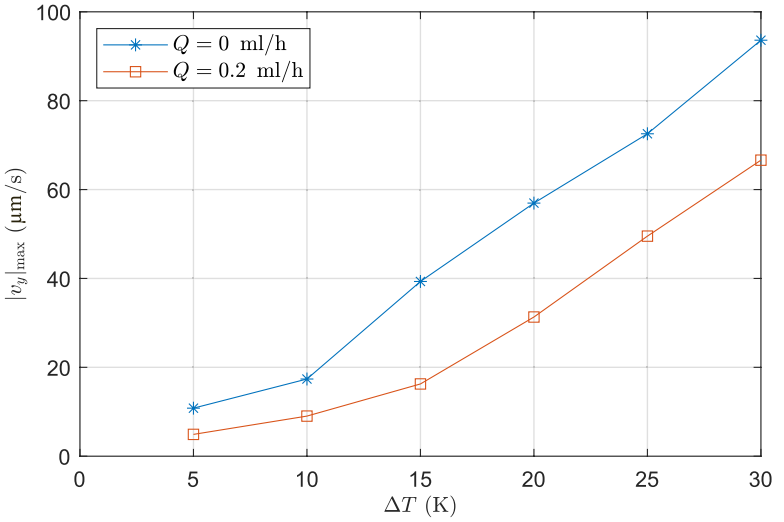

Figure 7. *Comparison of the magnitude of the transverse buoyancy-driven vortex, expressed as $|v_y|_{max}$, as a function of the ΔT, for the case without and with pressure-driven flow (Q = 0 and 0.2 ml/h).*

to the corresponding cases with mixed convection. This was consistently observed in all experiments, as shown in figure 7. In this plot, the differences in terms of absolute transverse velocity between the two configurations become clear. In all the cases with Q = 0 ml/h (blue line), $|v_y|_{max}$ is always larger than the corresponding case with Q = 0.2 ml/h (orange line). Interestingly, the difference becomes approximately constant for $\Delta T > 10$ K. This effect can be related to the improved heat transfer provided by the pressure-driven flow that reduces the effective temperature difference between the walls. Finally, the findings observed in figure 7 for the mixed convection case are summarised in table 1 in terms of the corresponding Reynolds number, $\mathrm{Re} = Q/(D_h \nu)$, Grashof number, $\mathrm{Gr} = g\beta\Delta T D_h^3/\nu^2$, Richardson number, $\mathrm{Ri} = \mathrm{Gr}/\mathrm{Re}^2$ and the non-dimensional transverse velocity $v^* = |v_y|_{\max}/|v_x|_{\max}$ (Hardt *et al*. 2006). The parameters ν and β are the kinematic viscosity and the coefficient of volume expansion of the fluid, respectively. It is interesting to notice that, although the large Ri indicates fully natural convection, the ratio between transverse and streamwise velocity shows that forced convection is of the same order as or larger order of magnitude than the natural convection, indicating that a mixed convection regime is established in the system.

4. Numerical analysis

This section focuses on the numerical analysis that was used to quantify the impact of the mixed convection on the mixing efficiency. Squared microchannels with six different diameters D_h are analysed

https://doi.org/10.1017/flo.2025.16 Published online by Cambridge University Press

under three different Reynolds numbers, Re = (0.1, 1, 10). The experimental results presented in the previous section were used for validation of the numerical code. The mixing efficiency of the cases with active mixing (swirl on) was evaluated with respect to the corresponding reference cases without mixed convection (swirl off).

4.1. Numerical methodology

The simulations were conducted with water as the working fluid, considered as a non-compressible and Newtonian fluid. The flow was assumed to be in a laminar regime under steady-state conditions. The computational analyses were performed utilising STAR-CCM+, a commercially available computational fluid dynamics software. This software employs the finite-volume method to solve the Navier–Stokes–Fourier equations. The set of governing equations employed in this study is reported below

$$\nabla \cdot (\rho \mathbf{u}) = 0, \tag{1}$$

$$\nabla \cdot (\rho \mathbf{u}\mathbf{u}) = -\nabla p + \mu \nabla^2 \mathbf{u} + \rho \mathbf{g}, \tag{2}$$

$$\nabla \cdot (\rho c_p T \mathbf{u}) = -\nabla \cdot (k \nabla T), \tag{3}$$

$$\nabla \cdot (\rho c \mathbf{u}) = -\nabla \cdot (D \nabla c). \tag{4}$$

Here, $\mathbf{u}$ is the flow velocity field, ρ is the fluid density, p is the pressure, T is the temperature, μ is the dynamic viscosity, k is the thermal conductivity coefficient and c_p is the specific thermal capacitance at constant pressure. The last equation represents the convection–diffusion equation, where c is a non-dimensional concentration and the diffusion coefficient D is taken equal to $2.8 \cdot 10^{-10}$ m^2/s, which corresponds to the diffusivity of a large dye molecule like Rhodamine B in water. The associated Schmidt number Sc is equal to 3180. The concentration c is normalised with respect to the maximum concentration of the Rhodamine, taking the value between 0 (pure water) and 1 (maximum/initial concentration in one half of the channel).

The computational domain was segmented into three distinct regions: the inlet region with a length $L_{in} = 15D_h$ where the thermal gradient is not applied, a central or active zone with a length $L = 50$ mm where the temperature gradient is applied and an outlet region with a length $L_{out} = 5$ mm used to avoid reversed flow in the central domain (see figure 1). The length of the inlet region was chosen to be dependent on the hydraulic diameter to facilitate comparisons between different geometries of the channel since the diffusive mixing is also active in the region without thermal mixing. With this choice, for different geometries and a fixed Reynolds number, the levels of mixing achieved at the entrance of the active zone will be the same.

The origin of the reference frame is located at the beginning of the active region. The mesh utilised in this study consisted of a structured grid composed of uniform hexahedral elements. A sensitivity analysis based on the relative error calculated with respect to the finest grid (6.4 million cells) of the v_y value across a line at $z = 0$ in the centre of the channel was performed to determine the optimal number of grid elements. The results, reported in figure 8, showed that 1.22 million elements, corresponding to 26×26 elements on the inlet plane, were sufficient to achieve mesh convergence. Regarding the flow boundary conditions, a fully developed Poiseuille velocity profile was prescribed at the inlet ($x = -L_{in}$), while an outflow condition was applied at the outlet ($x = L + L_{out}$). The fluid enters the domain at ambient temperature ($T_{in} = 303.15$ K). Concerning the thermal boundary conditions for the channel walls, both in the inlet and outlet passive zones, the walls are considered adiabatic. In the central region, Dirichlet boundary conditions were applied at the walls to produce the necessary temperature gradient. The wall at $y = +D_h/2$ was set to T_{hot} and the wall at $y = -D_h/2$ to T_{cold}. Throughout all simulations, T_{cold} and T_{hot} were kept constant at 293.15 K and 353.15 K, respectively, and with a temperature gradient between the two walls equal to $\Delta T/D_h = 50$ K/mm. The top ($z = +D_h/2$) and bottom ($z = -D_h/2$) channel walls were treated as adiabatic surfaces. It is crucial to note that the gravity vector points in the

https://doi.org/10.1017/flo.2025.16 Published online by Cambridge University Press

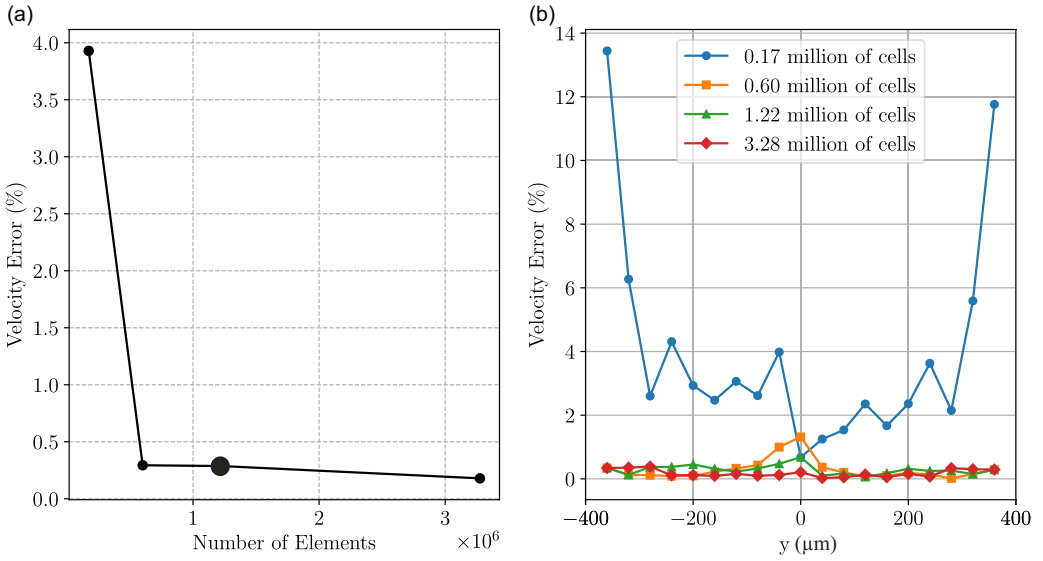

Figure 8. *Sensitivity analysis of the mesh on the v_y. (a) Relative velocity error as a function of the number of elements. The selected mesh with 1.22 million elements (highlighted with a larger marker) exhibits a similar error to the finest grid. (b) Error distribution along the considered line. Also in this case, the grid with 1.22 million elements follows a similar trend to the finest meshes.*

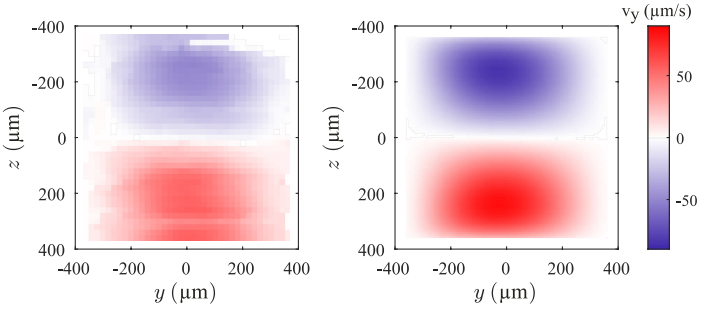

Figure 9. *Comparison between the v_y field from the experimental and numerical analyses for the case with Re = 1 and ΔT = 20 K.*

negative z-direction, defined as $\mathbf{g} = (0,0,-9.81)$ m/s^2. Additionally, all the thermophysical and transport properties of the fluid are modelled as functions of temperature following the International Association for the Properties of Water and Steam (IAPWS) model (Wagner & Kretzschmar 2008).

4.2. Numerical results

First, the numerical results were compared with the experimental measurements for validation, showing a good agreement in the distribution and magnitude of the transverse vortex. The case with Re = 1 and ΔT = 20 K is presented in figure 9.

For the mixing analysis, we considered the distribution of the non-dimensional concentration c. At the inlet, we arbitrarily chose to put the mixture of water and Rhodamine at maximum concentration ($c = 1$) in the half-channel region close to the hot wall ($y < 0$) and the pure water ($c = 0$) in the other region ($y > 0$). Figure 10 shows some exemplary concentration fields, taken in a plane in the centre of the channel ($z/D_h = 0$) for different Re values and D_h = 800 μm. The figure provides a qualitative comparison between the swirl-on and swirl-off cases. The swirl-off cases were obtained at the same

https://doi.org/10.1017/flo.2025.16 Published online by Cambridge University Press

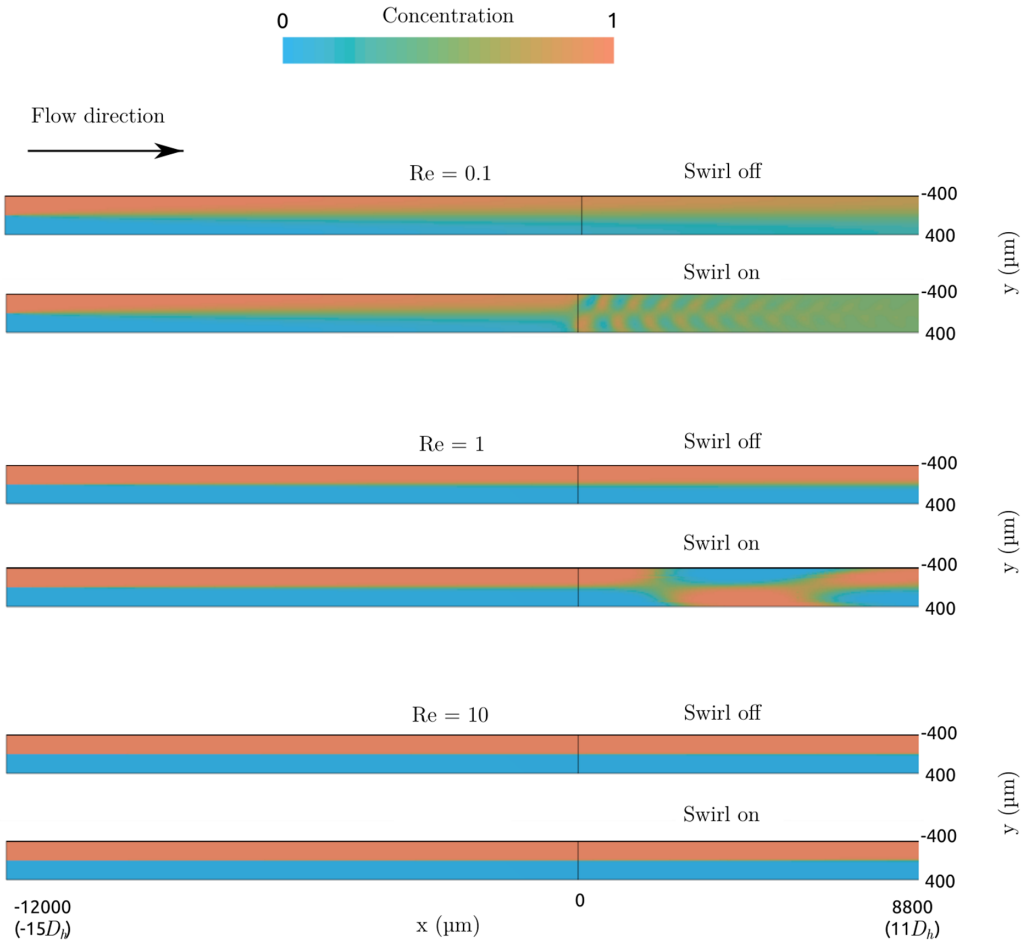

Figure 10. *Concentration maps obtained from numerical simulations for different values of Reynolds number (0.1,1 and 10).*

conditions (temperature, flow rate) but removing the gravitational field. As expected, in the swirl-off cases the mixing mechanism is slow and relies only on diffusion. When the swirl is activated (swirl on), the contact surface between the two fluids increases, thus improving mixing. Since the swirl magnitude is fixed by the , the active mixing (swirl on) is more effective at low Re. At larger Re, where the magnitude of the transverse flow is small compared with the streamwise velocity, the difference between the swirl-on and swirl-off cases is negligible.

The mass transport enhancement can be characterised by introducing a mixing efficiency parameter (ϕ), defined as

$$\phi = 1 - \frac{\sum_{i=1}^{n_{el}} |c_i - \bar{c}|}{2|\bar{c}|n_{el}}, \tag{5}$$

where c_i is the value of the non-dimensional concentration of the tracking fluid evaluated in the ith element of a certain cross-section, $\bar{c}$ is the average value of the concentration in the considered cross-section (here always equal to 0.5 for the mass conservation) and n_{el} is the number of elements of the cross-section. A value of $\phi = 1$ corresponds to a complete mixing. This parameter and the pressure drop Δp were analysed for different geometries (D_h) and Reynolds numbers (Re). Each result was compared with the respective reference swirl-off case, indicated with the subscript 0.

https://doi.org/10.1017/flo.2025.16 Published online by Cambridge University Press

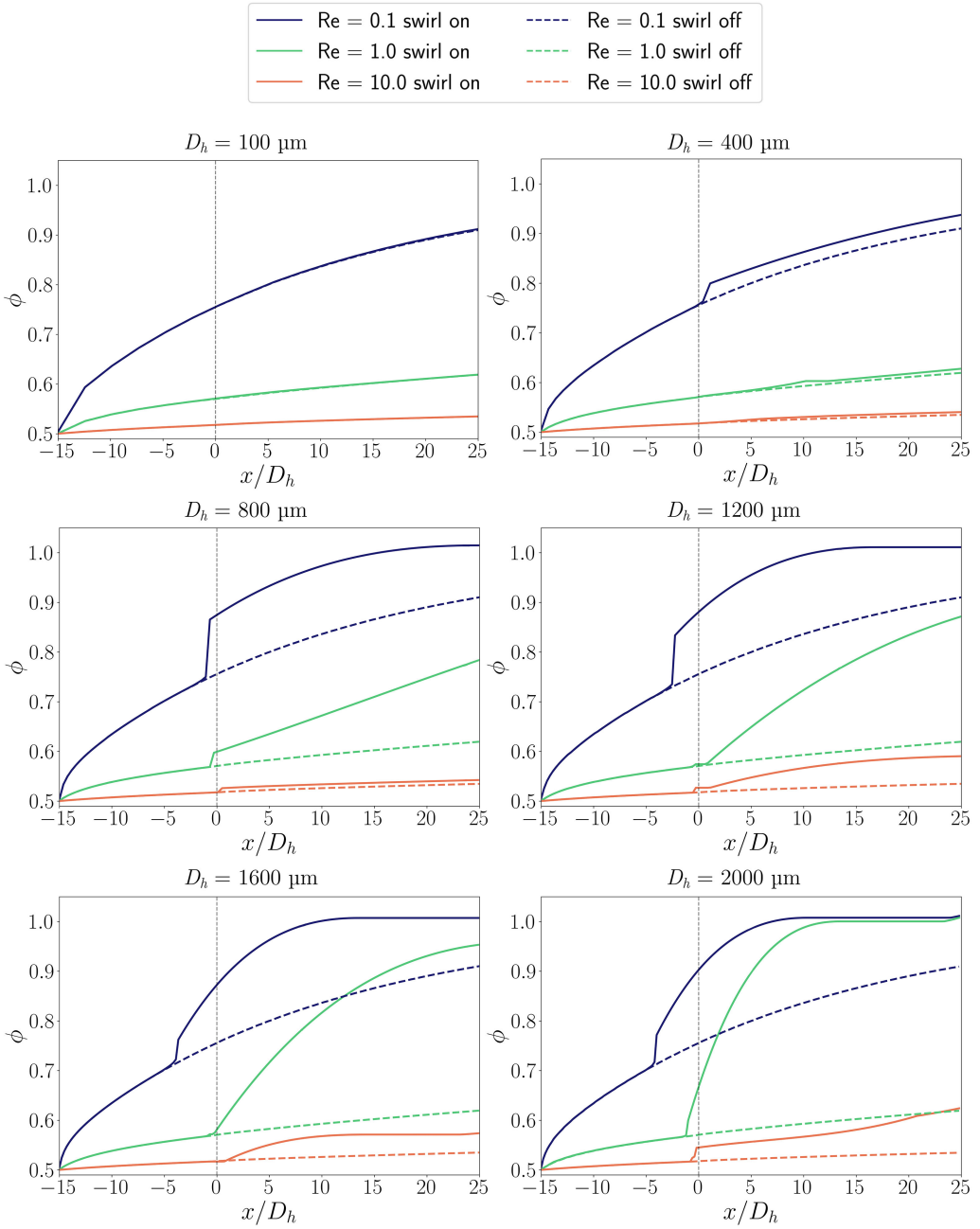

Figure 11. *Mixing efficiency ϕ against the dimensionless position x/D_h for different Reynolds numbers and different hydraulic diameters (D_h); the black dashed line refers to the beginning of the active region, always located at $x/D_h = 0$.*

In figure 11 we present the evolution of the mixing efficiency parameter ϕ in Eq. (5), evaluated across the capillary length for different hydraulic diameters and Re values. The streamwise direction was normalised with the hydraulic diameter of the channel (x/D_h), with the position $x/D_h = 0$ corresponding to the entrance of the active region (where the temperature gradient is activated). The results are presented from $x/D_h = -15$, which is the beginning of the inlet region, up to $x/D_h = 25$. Using this scaling, it is possible to compare the performance of different microchannels with different hydraulic diameters. The

https://doi.org/10.1017/flo.2025.16 Published online by Cambridge University Press

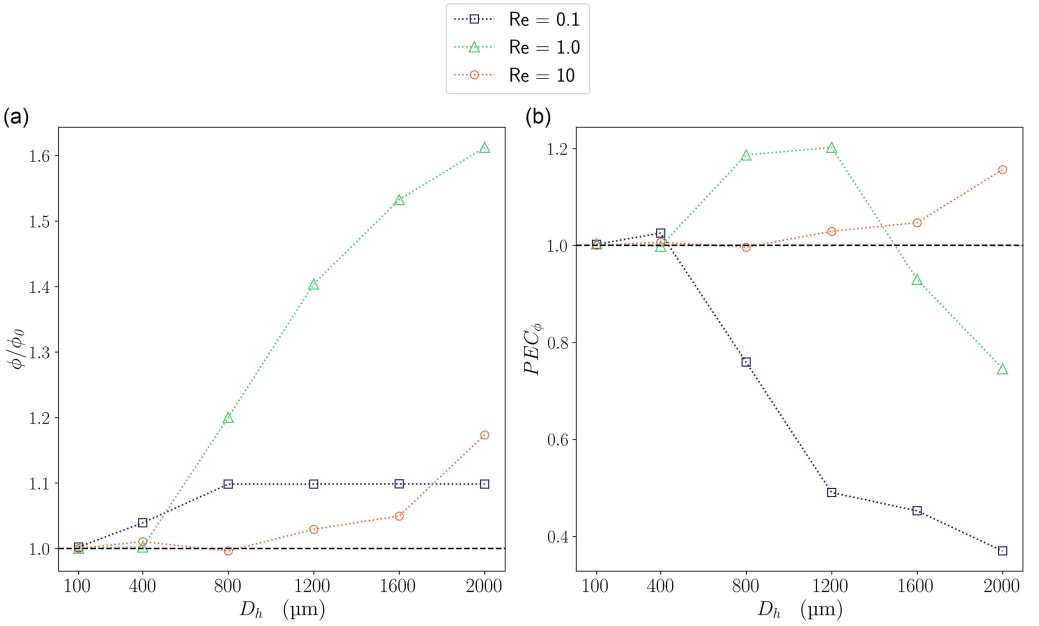

Figure 12. *(a) Value of ϕ at $x/D_h = 25$ as a function of the hydraulic diameter for the different Reynolds numbers. (b) Mixing efficiency parameter PEC_ϕ as a function of the hydraulic diameter for the different Reynolds numbers.*

black dashed line, shown in figure 11, refers to the starting point of the active region. For the smallest diameter $D_h = 100$ μm, the swirling effect is almost negligible since viscous forces dominate over buoyancy forces; the mixing is due to pure molecular diffusion and the concentration evolution is the same for the swirl-on and swirl-off cases. For all the other cases, the effect of the swirling is not negligible, and one can appreciate a clear enhancement of the mixing of the fluid for all the Reynolds numbers after the fluid enters the active region. The higher mixing efficiencies at the exit of the channel are observed, as expected, for the lower Reynolds numbers due to the larger residence time of the fluid in the channel. Interestingly, for the cases with larger D_h, the mixing enhancement starts before the active region (before the dashed red line), up to 5 times the hydraulic diameter of the capillary. This is linked to the backward propagation of the swirling motion from the active region, which becomes more effective as the D_h is increased.

A meaningful insight into the overall mixing efficiency is obtained by comparing the swirl-on and swirl-off mixing efficiency ratio (ϕ/ϕ_0) at the reference distance $x/D_h = 25$, as a function of D_h and parametrised with the Reynolds number. As illustrated in figure 12a, when the swirling is activated the mixing is always enhanced. This is true for all the cases analysed except for the smaller channel case ($D_H = 100$ μm), where the convective motion in the flow is not activated.

Even if the general trend of mass transport enhancement is clear, the mixing efficiency ratio behaviour is nonlinear with respect to Re. For the cases with a low Reynolds number (Re = 0.1), the value of ϕ/ϕ_0 as a function of D_h reaches an asymptotic value for $D_h \geq 800$ μm, showing that the complete mixing has been achieved already before $x/D_h = 25$. On the other hand, the asymptotic value of ϕ/ϕ_0 is equal to 1.1, showing that the effective mixing enhancement introduced by mixed convection is limited for low Re. At larger Reynolds numbers (Re = 10), the diffusion and the swirl magnitude are small compared with the streamwise advection, and ϕ/ϕ_0 remains low as well. To achieve good mixing, a longer channel length is required, and the mixing efficiency starts to increase effectively only for the larger hydraulic diameters, with negligible enhancement observed for $D_h < 1200$ μm. The most significant improvement was observed for the case of Re = 1, where, for $D_h = 2000$ μm, the swirling motion has more than 60 % mixing enhancement.

https://doi.org/10.1017/flo.2025.16 Published online by Cambridge University Press

Finally, to have a clearer picture with respect to the advantages of using the thermally induced swirling motion for mass transport enhancement, it is of interest to check the mechanical energy needed to drive the pressure-driven flow (i.e. the pressure drop Δp), which increases as the swirl magnitude is increased. A comparison was performed by analysing the performance efficiency parameter given by

$$PEC_\phi = \frac{\phi}{\phi_0} \Big/ \left(\frac{\Delta p}{\Delta p_0}\right)^{1/3}, \tag{6}$$

where the subscript 0 refers to the swirl-off case (Figure 12b). A value of $PEC_\phi > 1$ means that the mass transfer enhancement is predominant with respect to the pressure-drop increase, corresponding to a net overall enhancement of the efficiency of the system. One can readily see that, for the cases where swirling is present and large compared with streamwise advection (low Re), one needs to exert higher pumping power with respect to swirl-off flows, resulting in a low PEC_ϕ. Also for the case of large Re, the PEC_ϕ is larger than one only for larger channels with $D_h > 1600$ μm, therefore moving outside the microfluidic application.

In conclusion, from a fluid dynamic perspective, we can approximate the swirling flow to a superposition of a buoyancy-driven transverse vortex and a pressure-driven flow, that can be regulated independently by setting the temperature gradient and the flow rate. The transverse and streamwise flows remain essentially decoupled, although a larger buoyancy-driven vortex requires a larger pressure drop to sustain the streamwise flow. The mixing efficiency with respect to a molecular solute is promoted when the transverse velocities are large with respect to molecular diffusion and not too small with respect to the streamwise velocities. If these conditions are not verified, the mixing enhancement obtained with this approach is limited. For the fluid and temperature differences considered in this work, an optimal range of operation emerges for Re = 1 and D_h between 400 and 1600 μm. This range is particularly interesting from a technological point of view, since it covers microfluidic devices working at low flow rates, where diffusion is still too slow and active mixing is required.

5. Conclusions and recommendations

In this work, we studied the mixing efficiency of thermally driven microfluidic swirlers, i.e. active micromixers based on mixed thermal convection. In these mixers, a swirling motion is induced by a combination of the streamwise pressure-driven flow with a transverse buoyancy-driven flow. The buoyancy forces are introduced by a horizontal temperature gradient induced by Peltier modules in contact with the lateral walls of the microchannel. This active micromixer approach has several advantages since it is simple, does not require any movable parts and can easily be controlled and integrated into different microfluidic architectures.

We assessed the performance of a micromixer with a microchannel with a square cross-section of 800×800 μm^2 experimentally, using 3-D particle tracking. The analysis showed that, with temperature differences of the order of 20–30 K, a significant swirling motion with transverse velocity up to 90 μm/s can be established. The magnitude of the swirling flow is affected by the streamwise advection, showing smaller values when a pressure-driven flow is imposed. Furthermore, we performed a thorough systematic analysis of the efficiency of this mixing concept using numerical simulation for different Reynolds numbers (Re = 0.1, 1, 10) and hydraulic diameters (D_h between 100 and 2000 μm). The mixing was evaluated in terms of a mixing efficiency parameter ϕ and a performance efficiency parameter PEC_ϕ which also considers the pressure drop. The analysis revealed an optimal range of operation for this approach for microchannels with a hydraulic diameter between 400 and 1600 μm and a Reynolds number around 1. For smaller diameters or Reynolds numbers, the buoyancy forces become negligible, whereas for larger Re, the streamwise advection becomes dominant.

In conclusion, mixed convection can be used as an optimal active mixing approach in microfluidic devices working with conventional microchannel dimensions ($D_h \sim 0.4$–1.6 mm) and moderate flow velocities (Re ~ 1). Future follow-up investigations should address the impact in the mixing enhancement of different configurations of the temperature gradients, such as periodic inversion of temperature

https://doi.org/10.1017/flo.2025.16 Published online by Cambridge University Press

gradients in space (e.g. with staggered Peltier modules) or in time. In addition, recent works have already shown how the variation of thermophysical properties generated by a temperature gradient in a fluid, in combination with ultrasonic radiation, can create strong streaming flows (Qiu *et al*. 2021). The combination of acoustic and thermal effects in the presented system could easily be implemented, for instance by inducing vibration in the Peltier cells in contact with the channel. The interaction between acoustically induced streaming and buoyancy-driven swirling motion is expected to have a significant impact in enhancing the mixing performance and to extend the range of operation at larger Reynolds numbers.

Supplementary material. The supplementary material for this article can be found at https://dx.doi.org/10.1017/flo.2025.16.

Acknowledgements. Not applicable.

Data availability statement. Raw data are available from the corresponding author (M.R.) on request.

Author contributions. Conceptualisation: F.A, M.R.C. and M.R.; Methodology: F.A., M.R.C. and M.R.; Software: F.A and M.R.; Validation: F.A. and A.M.; Formal analysis: F.A., and A.M.; Investigation: F.A. and A.M.; Resources: B.P., G.L.M. and M.R.; Data curation: F.A. and A.M.; Writing – original draft: A.F. and A.M.; Writing - review and editing: M.E.G, M.R.C., B.P, G.L.M and M.R.; Visualisation: A.F.; Supervision: M.E.G., M.R.C., B.P, G.L.M and M.R.; Funding acquisition: G.L.M.

Funding statement. M.R.C. gratefully acknowledges the University of Bologna for the "2022 DIN Young Visiting Professor Fellowship" mobility award, which facilitated this fruitful collaboration. A.M. gratefully acknowledges the "DrEam" program from University of Lorraine.

Competing interests. The authors declare no conflict of interest.

Ethical standard. The research meets all ethical guidelines, including adherence to the legal requirements of the study country.

References

Amar, K., Embarek, D., & Sofiane, K. (2020). Parametric study of the crossing elongation effect on the mixing performances using short two-layer crossing channels micromixer (tlccm) geometry. *Chemical Engineering Research and Design*, *158*, 33–43.

Ansari, M. A., Kim, K., & Kim, S. M. (2018). Numerical and experimental study on mixing performances of simple and vortex micro t-mixers. *Micromachines*, *9*(5), 204.

Barnkob, R., Cierpka, C., Chen, M., Sachs, S., Mäder, P., & Rossi, M. (2021). Defocus particle tracking: A comparison of methods based on model functions, cross-correlation, and neural networks. *Measurement Science and Technology*, *32*(9), 094011.

Barnkob, R., Kähler, C. J., & Rossi, M. (2015). General defocusing particle tracking. *Lab on a Chip*, *15*(17), 3556–3560.

Barnkob, R., & Rossi, M. (2020). General defocusing particle tracking: Fundamentals and uncertainty assessment. *Experiments in Fluids*, *61*(4), 1–14.

Barnkob, R., & Rossi, M. (2021). Defocustracker: A modular toolbox for defocusing-based, single-camera, 3D particle tracking. *Journal of Open Research Software*, *9*(1), 22.

Bayareh, M., Usefian, A., & Ahmadi Nadooshan, A. (2019). Rapid mixing of Newtonian and non-Newtonian fluids in a three-dimensional micro-mixer using non-uniform magnetic field. *Journal of Heat and Mass Transfer Research*, *6*(1), 55–61.

Cai, G., Xue, L., Zhang, H., & Lin, J. (2017). A review on micromixers. *Micromachines*, *8*(9), 274.

Capretto, L., Cheng, W., Hill, M., & Zhang, X. (2011). Micromixing within microfluidic devices. *Microfluidics: Technologies and applications*, *304*, 27–68.

Coutinho, G., Moita, A., Ribeiro, A., Moreira, A., & Rossi, M. (2023). On the characterization of bias errors in defocusing-based 3d particle tracking velocimetry for microfluidics. *Experiments in Fluids*, *64*(5), 106.

Ebrahimi, S., Hasanzadeh-Barforoushi, A., Nejat, A., & Kowsary, F. (2014). Numerical study of mixing and heat transfer in mixed electroosmotic/pressure driven flow through t-shaped microchannels. *International Journal of Heat and Mass Transfer*, *75*, 565–580.

Hardt, S., Pennemann, H., & Schönfeld, F. (2006). Theoretical and experimental characterization of a low-Reynolds number split-and-recombine mixer. *Microfluidics and Nanofluidics*, *2*(3), 237–248.

Hong, S. O., Park, K., Kim, D., Lee, S. S., Lee, C., & Kim, J. M. (2021). Gear-shaped micromixer for synthesis of silica particles utilizing inertio-elastic flow instability. *Lab on a Chip*, *21*(3), 513–520.

Hsieh, S., Lin, J., & Chen, J. (2013). Mixing efficiency of y-type micromixers with different angles. *International Journal of Heat and Fluid Flow*, *44*, 130–139.

Ishii, K., Hihara, E., & Munakata, T. (2020). Mechanism of temperature-difference-induced spiral flow in microchannel and investigation of mixing performance of a non-invasive micromixer. *Applied Thermal Engineering*, *174*, 115291.

Ishii, K., Someya, S., & Munakata, T. (2018). Investigation of temperature-induced flow stratification and spiral flow in T-shaped microchannel. *Microfluidics and Nanofluidics*, *22*(9), 1–10.

Jiang, F., Drese, K. S., Hardt, S., Küpper, M., & Schönfeld, F. (2004). Helical flows and chaotic mixing in curved micro channels. *AIChE Journal*, *50*(9), 2297–2305.

Kim, S.-J., Wang, F., Burns, M. A., & Kurabayashi, K. (2009). Temperature-programmed natural convection for micromixing and biochemical reaction in a single microfluidic chamber. *Analytical Chemistry*, *81*(11), 4510–4516.

Li, Z., & Kim, S. (2017). Pulsatile micromixing using water-head-driven microfluidic oscillators. *Chemical Engineering Journal*, *313*, 1364–1369.

Li, Z., Zhang, B., Dang, D., Yang, X., Yang, W., & Liang, W. (2022). A review of microfluidic-based mixing methods. *Sensors and Actuators A: Physical*, *344*, 113757.

Lim, E., Lee, L., Yeo, L. Y., Hung, Y., & Tan, M. (2019). Acoustically driven micromixing: Effect of transducer geometry. *IEEE Transactions on Ultrasonics, Ferroelectrics, and Frequency Control*, *66*(8), 1387–1394.

Milotin, R., & Lelea, D. (2016). The passive mixing phenomena in microtubes with baffle configuration. *Procedia Technology*, *22*, 243–250.

Picardo, J. R., & Pushpavanam, S. (2015). Laterally stratified flow in a curved microchannel. *International Journal of Multiphase Flow*, *75*, 39–53.

Qiu, W., Joergensen, J. H., Corato, E., Bruus, H., & Augustsson, P. (2021). Fast microscale acoustic streaming driven by a temperature-gradient-induced nondissipative acoustic body force. *Physical Review Letters*, *127*(6), 064501.

Rallabandi, B., Wang, C., & Hilgenfeldt, S. (2017). Analysis of optimal mixing in open-flow mixers with time-modulated vortex arrays. *Physical Review Fluids*, *2*(6), 064501.

Schönfeld, F., & Hardt, S. (2004). Simulation of helical flows in microchannels. *AIChE Journal*, *50*(4), 771–778.

Stroock, A. D., Dertinger, S. K., Ajdari, A., Mezic, I., Stone, H. A., & Whitesides, G. M. (2002). Chaotic mixer for microchannels. *Science*, *295*(5555), 647–651.

Tan, H. (2019). Numerical study of a bubble driven micromixer based on thermal inkjet technology. *Physics of Fluids*, *31*(6), 062006.

Wagner, W., & Kretzschmar, H.-J. (2008). IAPWS industrial formulation 1997 for the thermodynamic properties of water and steam. In *International Steam Tables* (pp. 7–150). Springer, Berlin, Heidelberg.

Wang, W., Zhao, S., Shao, T., Jin, Y., & Cheng, Y. (2012). Visualization of micro-scale mixing in miscible liquids using μ-lif technique and drug nano-particle preparation in t-shaped micro-channels. *Chemical Engineering Journal*, *192*, 252–261.

Ward, K., & Fan, Z. H. (2015). Mixing in microfluidic devices and enhancement methods. *Journal of Micromechanics and Microengineering*, *25*(9), 094001.

Whitesides, G. M. (2006). The origins and the future of microfluidics. *Nature*, *442*(7101), 368–373.

Zhang, K., Ren, Y., Hou, L., Tao, Y., Liu, W., Jiang, T., & Jiang, H. (2020). Continuous microfluidic mixing and the highly controlled nanoparticle synthesis using direct current-induced thermal buoyancy convection. *Microfluidics and Nanofluidics*, *24*(1), 1–14.

Zhang, S., Chen, X., Wu, Z., & Zheng, Y. (2019). Numerical study on stagger Koch fractal baffles micromixer. *International Journal of Heat and Mass Transfer*, *133*, 1065–1073.

Cite this article: Azzini F., M'hadbi A., El Ganaoui M., Pulvirenti B., Morini G. L., Rojas-Cárdenas M. and Rossi M. (2025). Assessment of mixing efficiency of thermally driven microfluidic swirlers. *Flow*, *5*, E21. https://doi.org/10.1017/flo.2025.16